Japanese Journal of Applied Physics
Vol. 46, No. 7B, 2007, pp. 4873–4880

Measurement of Angular Dependence of Ultrasonic Echo for Estimation of Surface Roughness

Kazuki KUDO, Hideyuki HASEGAWA, and Hiroshi KANAI*

Graduate School of Engineering, Tohoku University, Sendai 980-8579, Japan

(Received November 24, 2006; accepted March 22, 2007; published online July 26, 2007)

Atherosclerosis is the main cause of circulatory diseases, and it is very important to diagnose atherosclerosis in its early stage. In an early stage of atherosclerosis, the luminal surface of an arterial wall becomes rough due to injury of the endothelium. Conventional ultrasonic diagnostic equipments cannot detect such micron-order surface roughness because their spatial resolution is, at most, 100 μm. In this study, for the accurate detection of surface roughness, ultrasonic beams were insonified from various angles relative to the surface of an object that has a micron-order asperity. Then, we focused on the angular dependence of echo amplitude and frequency characteristics in both temporal and spatial domains. Using this method, it is shown that the angular dependence and frequency characteristics vary when an object has a surface roughness that cannot be detected by conventional B-mode imaging using linear scanning. [DOI: 10.1143/JJAP.46.4873]

KEYWORDS: surface roughness, ultrasonic beam steering, angular dependence, temporal and spatial frequency, atherosclerosis

1. Introduction

Recently, the increases in the number of circulatory diseases such as myocardial and cerebral infarctions have become a serious problem. Therefore, it is important to diagnose atherosclerosis in an early stage because such circulatory diseases are mainly caused by atherosclerosis. For the diagnosis of atherosclerosis, intima-media thickness is a useful marker.[1)] Mashiyama *et al.* measured the intima-media thickness at the carotid sinus, which is a site that is easily affected by atherosclerosis, by beam steering that makes all ultrasonic beams perpendicular to the arterial wall.[2)] Furthermore, the evaluation of the elasticity of an arterial wall is also useful for the diagnosis of atherosclerosis,[3)] and the measurement of the regional elasticity of an arterial wall using the *phased tracking method* was reported.[4,5)] This method was applied for classification of tissues in the arterial wall on the basis of the statistical properties of elasticity distribution.[6–8)]

Although these methods are useful for the diagnosis of atherosclerotic changes of the intima-media region, the initial step of atherosclerosis development was reported to be endothelial damage.[9)] Therefore, for the diagnosis of atherosclerosis in an early stage, it is more effective to evaluate endothelial damage. For the evaluation of endothelial function, several methods have been reported including the measurement of changes in diameter[10)] and intima-media elasticity[11)] caused by flow-mediated dilation. In these methods, the measured changes in diameter or intima-media elasticity are caused by the response of the media to nitric oxide generated by the endothelium. Therefore, if the endothelium is injured, the response of the media to nitric oxide generated by the endothelium does not occur.

In the early stage of atherosclerosis, it was also reported that the luminal surface profile changes. The luminal surface of a clinically healthy artery is covered by a layer composed of endothelial cells and it is smooth. In the early stage of atherosclerosis, endothelial cells on the luminal surface are damaged,[9)] edema develops under the endothelium, endothelial cells are separated from the intima, and then the lumen of the artery has a micron-order surface roughness.[12)] Therefore, for the detection of atherosclerosis in an early stage, it is necessary to detect a micron-order surface roughness on the luminal surface. In conventional ultrasonic diagnostic equipments, the lateral interval of ultrasonic beams is, at most, 100 μm, and the axial resolution of a B-mode image depends on the ultrasonic wavelength of 150 μm at 10 MHz because a B-mode image is constructed using the amplitude of the received echo. From these facts, the spatial resolution of a B-mode image obtained using ultrasonic diagnostic equipment is, at most, 100 μm in both lateral and axial directions. Therefore, the surface roughness caused by atherosclerosis in an early stage cannot be detected by conventional B-mode imaging using ultrasonic diagnostic equipment. There are several studies of the ultrasonic detection of micron-order surface roughness. Sukmana *et al.* measured the surface roughness of sandpaper using air-coupled ultrasound, and showed that higher-frequency components in echo are attenuated when the surface of the object has a micron-order surface roughness.[13,14)] Arihara *et al.* measured the micron-order surface profile of an object made of silicone rubber using the phase of RF echo.[15)] However, these methods are still not sufficient for accurate imaging of a surface with micron-order asperity.

In this study, various objects of different micron-order surface profiles were measured to obtain the angular dependences of ultrasonic echoes. Ultrasonic beams were insonified from various angles relative to the surface of an object that has micron-order asperity. Then, for the evaluation of micron-order surface roughness, we focused on the angle-dependent characteristics of echo amplitude and frequency characteristics in both temporal and spatial domains.

2. Principles

2.1 Data acquisition

Figures 1(a) and 1(b) show the schematic views of the experimental system and beam scanning, respectively. A linear-type ultrasonic probe (center frequency $f_0 = 10$ MHz, interval of aperture centers for transmitted beams $L = 0.4$ mm) of conventional ultrasonic diagnostic equipment (Aloka SSD-6500) is used in this study. The number of electronically scanned beams, N, is 30 per frame. Ultrasonic RF echoes are sampled at 40 MHz with a 16-bit resolution.

*E-mail address: hkanai@ecei.tohoku.ac.jp

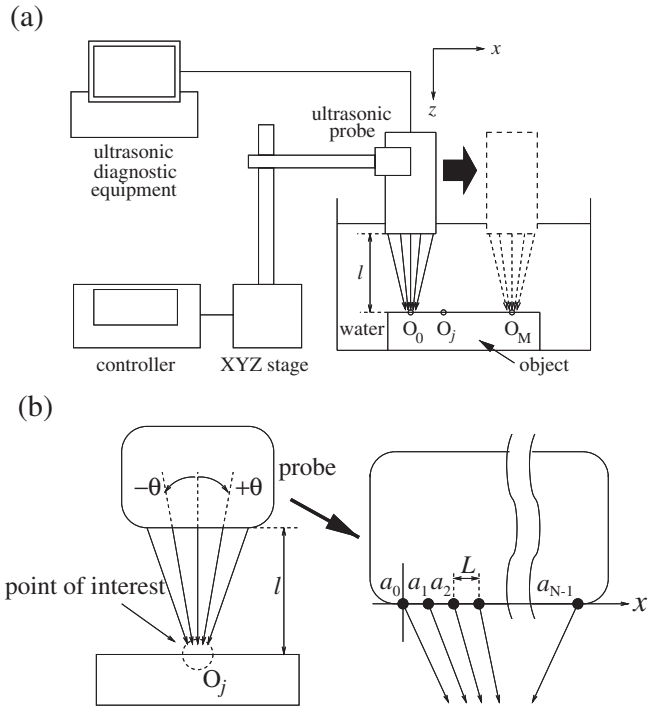

Fig. 1. (a) Experimental system for measurement of an object surface. (b) Schematic diagram of beam scanning.

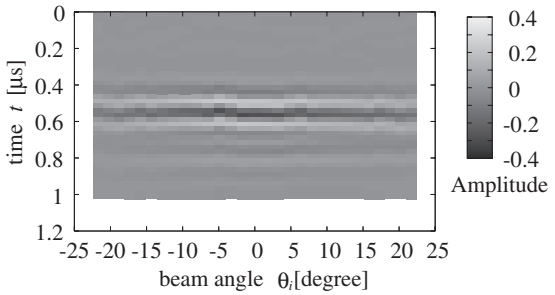

Fig. 2. RF echo from a point scatterer at each beam angle θ_i.

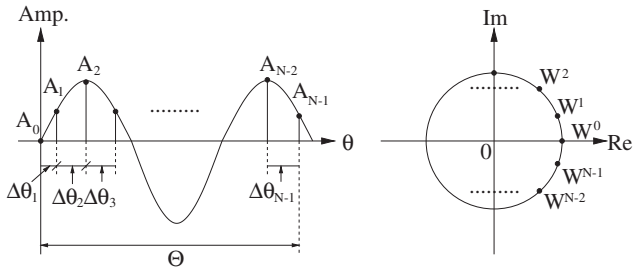

Fig. 3. Schematic diagram of the unequally spaced discrete Fourier transform.

The method using steering the ultrasonic beam proposed by Nakagawa *et al.*[16] and shown in Fig. 1(b) is used in this study. Using this method, the direction of all ultrasonic beams can be designed so as to pass through a point of interest. As shown in Fig. 1(b), all beams pass through a point, O_j, at the surface of the object. When an ultrasonic beam is insonified from the position a_i of the aperture center i, the beam angle θ_i is expressed as follows:

$$\theta_i = \tan^{-1} \frac{L \cdot \left(i - \dfrac{N-1}{2} \right)}{l}. \tag{2.1}$$

The distance l from the surface of the probe to the surface of the object is set to be 13.7 mm, and then the maximum beam angle $\theta_{\max}$ is 24.3°.

Furthermore, the ultrasonic probe is used to scan the object by changing its position x_j using a stage in order to measure RF echo from multiple points of interest on the surface along the x-direction. At each position x_j in j-th frame ($j = 1, 2, \ldots, M$), all beams pass through a point O_j, which is set at the surface of the object. The position x_j is changed by 5 μm per frame for 2 s (frame rate: FR = 434 Hz, speed of stage motion: 2.17 mm/s).

2.2 *Analysis of angular dependence*

Figure 2 shows RF echo from a point scatterer at each beam angle θ_i. The amplitude of RF echo is normalized by the acoustic pressure that corresponds to the maximum 16-bit discrete value.

In this measurement, the distance from the point of interest to the receiving position varies as the beam angle θ_i changes. Thus, the propagation time t_i at each ultrasonic beam should be corrected by the difference in propagation distance. The propagation time t_i at a position a_i, where the ultrasonic beam is insonified, is given by

$$t_i = \frac{2l}{c \cdot \cos\theta_i}, \tag{2.2}$$

where c is the sound speed in water. As shown in Fig. 2, the waveform of RF echo is not distorted and the wavefront of the echo at each ultrasonic beam aligns in the case that the object is a point scatterer. Thus, received RF echoes at various beam angles are plotted as a function of the beam angle θ_i and the time t, which is corrected by the difference in propagation time.

In this study, for the more detailed analysis of received RF echo, the Fourier transform in the angle (θ) and time (t) domains was applied. However, as shown in eq. (2.1), the beam angle θ_i is assigned unequally spaced discrete values, while the sampling period in the time domain is assigned equally spaced values. Therefore, the spatial frequency spectrum should be obtained by the unequally spaced discrete Fourier transform (DFT) in the θ-direction. Figure 3 shows a schematic diagram of unequally spaced DFT and the twiddle factor $W(i)$. When a sampling interval between the $(i-1)$-th and i-th beams in the θ-direction is defined as $\Delta\theta_i$ ($\Delta\theta_0$ is defined as 0), the twiddle factor $W(i)$ is obtained as follows:

$$W(i) = \exp\left(-j \frac{2\pi}{\Theta} \sum_{n=0}^{i} \Delta\theta_n \right) \quad (i = 1, 2, \ldots, N-1), \tag{2.3}$$

where Θ is the signal length in the θ-direction. Then, when an echo amplitude of at the i-th beam is defined as A_i shown in Fig. 3, the power spectrum $Y(u)$ is obtained as follows:

$$Y(u) = Y\left(\frac{i}{\Theta} \right) = \sum_{n=0}^{N-1} A_n (W(n))^i, \tag{2.4}$$

where u is the spatial frequency whose unit is defined as deg^{-1}. To prevent aliasing, the spatial frequency u must be less than $1/\Delta\theta_{\max}$ ($\Delta\theta_{\max}$ is the largest $\Delta\theta_i$).

(a)

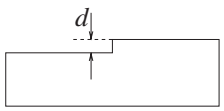

Object No.	d [μm]
1	35
2	57
3	90

(b)

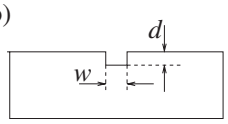

Object No.	d [μm]	w [μm]
4	30	62
5	58	64
6	33	120
7	60	122

Fig. 4. Surface profiles of the objects. (a) With steps. (b) With gaps.

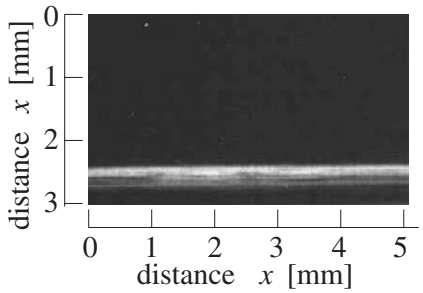

Fig. 5. B-mode image of object No. 1 (step: $d = 35\,\mu$m).

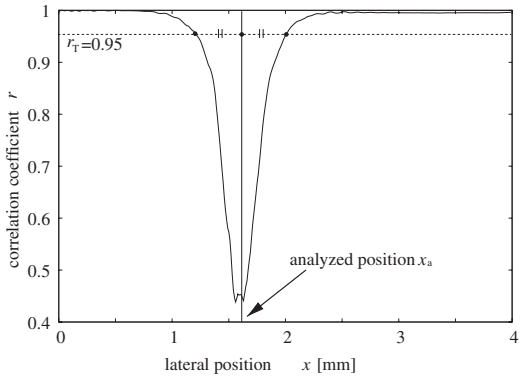

Fig. 7. Change in correlation coefficient of the angular dependence.

3. Basic Experiments

3.1 Determination of position of step or gap

Three different objects whose surfaces have single steps, as shown in Fig. 4(a), and four different objects whose surfaces have single gaps, as shown in Fig. 4(b), were used in basic experiments. These objects were made of aluminum, and their surfaces were flat except for the steps or gaps. As shown in Fig. 4, objects Nos. 1–3 have steps with different step heights, d, and objects Nos. 4–7 have gaps with different depths, d, and widths, w. Figure 5 shows a B-mode image of object No. 1 (step: $d = 35\,\mu$m) obtained using ultrasonic diagnostic equipment. As shown in Fig. 5, a step cannot be recognized by conventional B-mode imaging using linear scanning. Therefore, the position of a step or a gap, x_a, must be determined by a method other than conventional B-mode imaging.

For the determination of the position of a step or a gap, the angular dependence of the maximum amplitude of ultrasonic RF echo at each point of interest O_j was measured using the stage. As shown in Fig. 1(a), angular dependence was measured at each point of interest O_j by moving the ultrasonic probe, and the angular dependence is shown as a function of the beam angle θ_i and the lateral position x_j. Figure 6(a) shows the measured angular dependence of the maximum amplitude of object No. 1 (step: $d = 35\,\mu$m), and Fig. 6(b) shows the angular dependence at the position of the surface that is smooth ($x_j = 0\,\mu$m). As shown in Fig. 6(a), the angular dependence at the region where the surface has a step differs from that at the region where the surface does not have a step. Therefore, we focused our attention on the change in angular dependences to determine the position x_a of a step or a gap.

The change in the angular dependence at each point of interest is quantitatively evaluated by the correlation function between the angular dependence obtained at the smooth surface shown in Fig. 6(b) and that at each point of interest. In Fig. 7, the correlation coefficient of the angular dependence is plotted as a function of the lateral position x_j. As shown in Fig. 7, the correlation coefficient decreases at the region where the surface has a step, while the correlation coefficient is consistently more than $r_j = 0.99$ at the region where the surface is smooth. The position x_a of a step or a gap is supposed to be the median point of the positions where the correlation coefficient drops from $r_j \simeq 1$ and where the the correlation coefficient returns to $r_j \simeq 1$. Therefore, in this study, the median points of the position where the correlation coefficient falls below the threshold $r_T = 0.95$ were determined as the analyzed point x_a.

3.2 Angular dependence of echo from a step on a surface

Figures 8(a)–8(d) show RF echoes at the corresponding beam angles $\{\theta_i\}$ of an object with a smooth surface and the objects Nos. 1–3, respectively. As shown in Fig. 8, the waveform of the RF echo is not distorted and the wavefront of echo at each ultrasonic beam aligns when the point

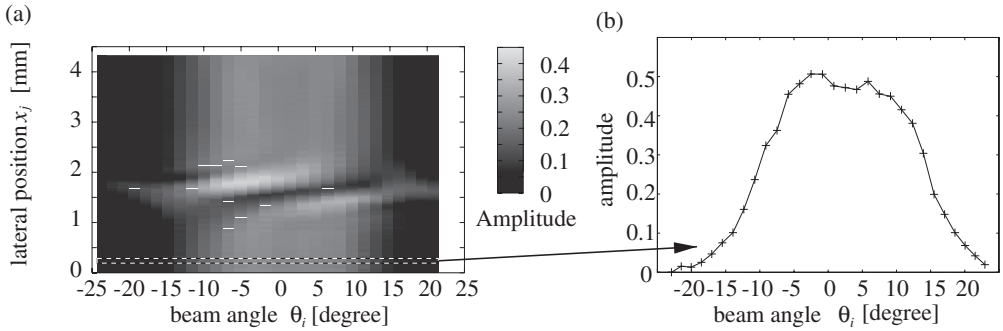

Fig. 6. (a) Angular dependence of maximum amplitude (object No. 1). (b) Angular dependence at a smooth surface.

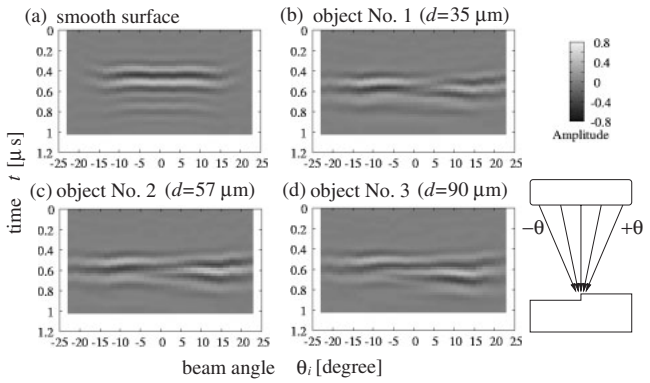

Fig. 8. RF echoes at corresponding beam angles θ_i. (a) Smooth surface. (b) $d = 35\,\mu$m. (c) $d = 57\,\mu$m. (d) $d = 90\,\mu$m.

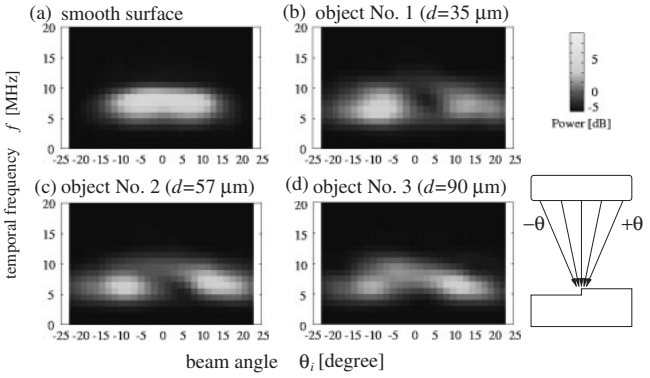

Fig. 9. Temporal frequency characteristic at each beam angle θ_i. (a) Smooth surface. (b) $d = 35\,\mu$m. (c) $d = 57\,\mu$m. (d) $d = 90\,\mu$m.

of interest is a smooth surface. On the other hand, the wavefronts of RF echoes are distorted and the echo amplitude decreases, particularly when the beam angle θ_i is about 0°, in the case that a point of interest is a position with a step.

Figure 9 shows the power spectrum of RF echo at each beam angle θ_i. As shown in Fig. 9, in the case of a smooth surface, the frequency component at $f = 7.5\,$MHz, which corresponds to the center frequency of RF echo from the point scatterer shown in Fig. 2, are maximum at most of the beam angles, and the power spectrum decreases as the beam angle θ_i increases. On the other hand, in the case that the point of interest is at the position with a step, the power spectra at $\theta_i \simeq \pm 10^\circ$ are higher than that of a smooth surface ($d = 0\,\mu$m). However, the power spectra are lower than that of $d = 0\,\mu$m when the beam angle θ_i is about 0°. Moreover, the power spectra where the beam angle θ_i is about -10° decrease as the step height d increases.

Figure 10 shows the two-dimensional spectrum of RF echo obtained by the two-dimensional Fourier transform of the RF echo obtained at each beam angle shown in Fig. 8. In Fig. 10, the power spectra are also represented in contours. As shown in Figs. 10(b)–10(d), the frequency components at $f = 7.5\,$MHz (center frequency) increase as the step height d increases, whereas the other frequency components does not increase so much. From these results, the bandwidth of the power spectrum of RF echo was found to be narrow in the temporal frequency domain as the step height d increases. It corresponds to the increment in the number of cycles of echo

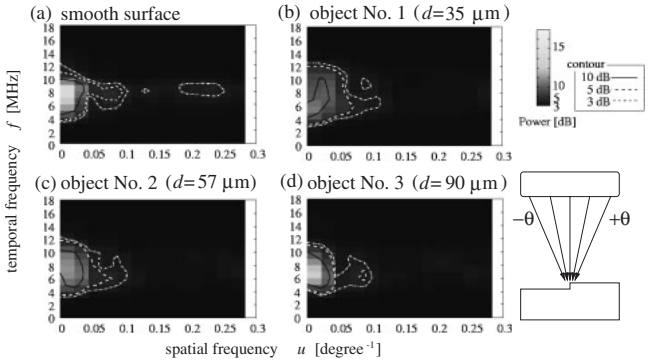

Fig. 10. 2-D power spectrum of RF echo. (a) Smooth surface. (b) $d = 35\,\mu$m. (c) $d = 57\,\mu$m. (d) $d = 90\,\mu$m.

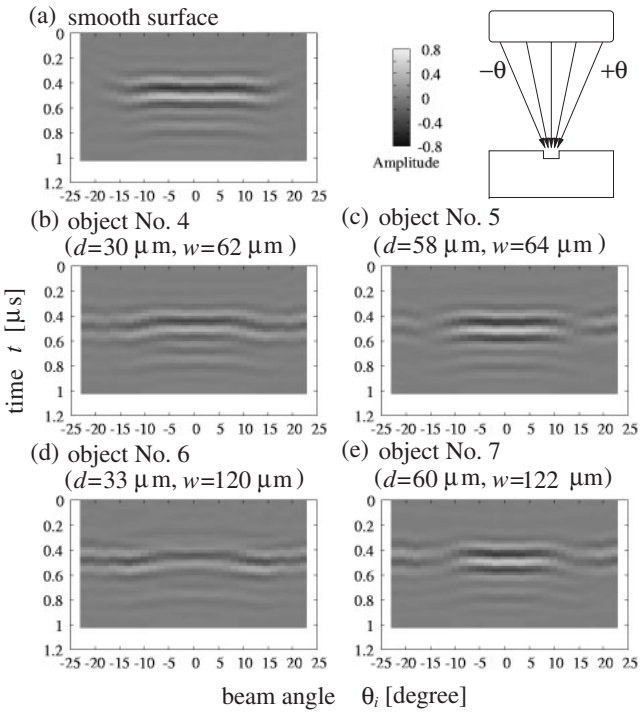

Fig. 11. RF echoes at corresponding beam angles θ_i. (a) Smooth surface. (b) $d = 30\,\mu$m, $w = 62\,\mu$m. (c) $d = 58\,\mu$m, $w = 64\,\mu$m. (d) $d = 33\,\mu$m, $w = 120\,\mu$m. (e) $d = 60\,\mu$m, $w = 122\,\mu$m.

in the temporal axis on the right-hand side of Figs. 8(a)–8(d). From these results, it is supposed that the bandwidth of the power spectrum of RF echoes is narrow in the temporal frequency domain as the step height d increases.

3.3 Angular dependence of echo from a gap on a surface

Figures 11(a)–11(e) show RF echoes at the corresponding beam angles $\{\theta_i\}$ of the object with a smooth surface and objects Nos. 4–7, respectively. In the case that the surface has a gap, the distortion of the wavefront of RF echo shown in Figs. 8(b)–8(c) does not occur. However, as shown in Fig. 11, the echo amplitudes in the range $|\theta_i| \geq 15^\circ$ are higher than that of the smooth surface, whereas in the case of the smooth surface, the echo amplitude is almost 0 when $|\theta_i| \geq 15^\circ$.

Figure 12 shows the power spectrum of RF echo at each beam angle θ_i. As shown in Fig. 12, when the surface has a gap, the power spectra where $|\theta_i|$ is greater than 15° increase as the gap width w increases. The supposed reason for the

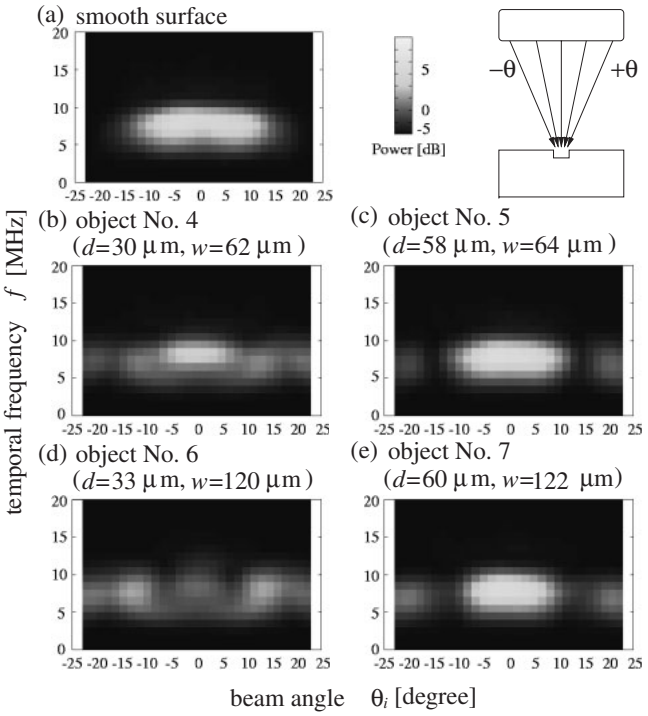

Fig. 12. Temporal frequency characteristic at each beam angle θ_i. (a) Smooth surface. (b) $d = 30\,\mu$m, $w = 62\,\mu$m. (c) $d = 58\,\mu$m, $w = 64\,\mu$m. (d) $d = 33\,\mu$m, $w = 120\,\mu$m. (e) $d = 60\,\mu$m, $w = 122\,\mu$m.

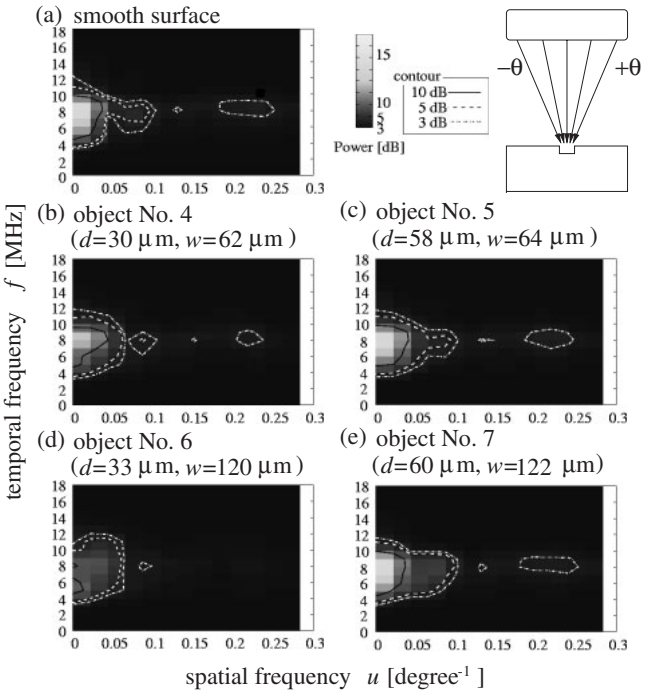

Fig. 13. 2-D power spectrum of RF echo. (a) Smooth surface. (b) $d = 30\,\mu$m, $w = 62\,\mu$m. (c) $d = 58\,\mu$m, $w = 64\,\mu$m. (d) $d = 33\,\mu$m, $w = 120\,\mu$m. (e) $d = 60\,\mu$m, $w = 122\,\mu$m.

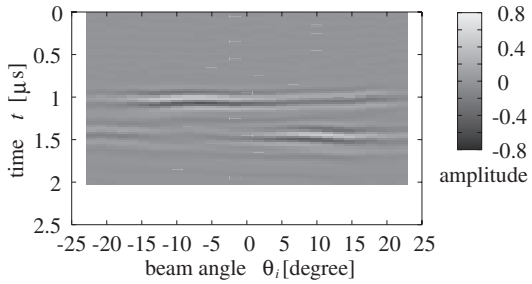

Fig. 14. RF echoes from a step ($d = 300\,\mu$m) at the corresponding beam angles.

increase in power spectra when $|\theta_i|$ is greater than 15° is that the effects of the gap on the power spectrum increase as the gap width w increases.

Figure 13 shows the two-dimensional spectrum of RF echo obtained by the two-dimensional Fourier transform of the spatial distribution of the echo amplitude shown in Fig. 11. As shown in Fig. 13, the power spectra are also represented in contours as in Fig. 10. As shown in Fig. 13, the components in the range of $0.05 \leq u \leq 0.10$ increases in the case of objects Nos. 5 and 7 whose gap depth d are larger than those of objects Nos. 4 and 6. This corresponds to the observation that the region along the θ-axis where the amplitude is high narrows. Therefore, it is supposed that the components at high frequencies in the spatial frequency domain increase as the gap depth d increases.

4. Discussion

4.1 Angular dependence of echo from a step on a surface

As shown in Fig. 8, RF echoes from a step at the corresponding beam angles of $\{\theta_i\}$ are asymmetrical owing to an asymmetric shape of a surface profile, while RF echoes from a gap are symmetrical. In addition, the angular dependence of a step has a characteristic that the number of cycles of echo in the temporal axis on the right-hand sides of Figs. 8(b)–8(d) increases as step height increases. To examine such a characteristic, another object was measured. This object has a step whose height d is 300 μm (d is sufficiently higher than ultrasonic wave length, $\lambda = 200$ μm). Figure 14 shows RF echoes at the corresponding beam angles $\{\theta_i\}$ of this object ($d = 300\,\mu$m). As shown in Fig. 14, at most of the beam angles $\{\theta_i\}$, the received signals contain echoes from the upper and lower surfaces around the step owing to a large beam diameter. Echo amplitudes from the lower surface of the step are high in the range $+5 \leq \theta \leq +15°$ and those are almost 0 in the range $-15 \leq \theta \leq -5°$. On the other hand, echo amplitudes from the upper surface of the step are high in the range $-15 \leq \theta \leq -5°$ and those are low in the range $+5 \leq \theta \leq +15°$. However, as shown in Fig. 14, echoes from the upper surface in the range $+5 \leq \theta \leq +15°$ do not decrease so much in comparison with those from the lower surface in the range $-15 \leq \theta \leq -5°$. This is considered to be a reason that echo duration in the range $+5 \leq \theta \leq +15°$ increased as observed in Figs. 8(b)–8(d), whereas that in the range $-15 \leq \theta \leq -5°$ did not increase.

4.2 Angular dependence of echo from a gap on a surface

In this study, the angular dependence of echo from a gap on a surface was measured in addition to that from a step. Let us consider the angular dependences of echoes from a gap on a surface by summing up those from steps. Figure 15 shows a schematic diagram for simulating a shape of a gap using a shape of a step on the basis of the superposition principle. In this study, the employed objects have a step d of about 30 or 60 μm and a gap width w of 60 or 120 μm. Therefore, the angular dependences of echoes from a gap

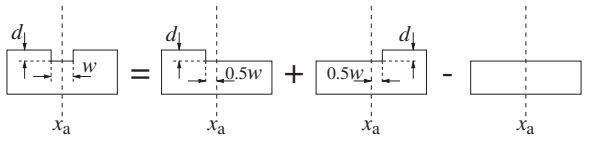

Fig. 15. Schematic diagram for simulation of a shape of a gap by summing up shapes of steps.

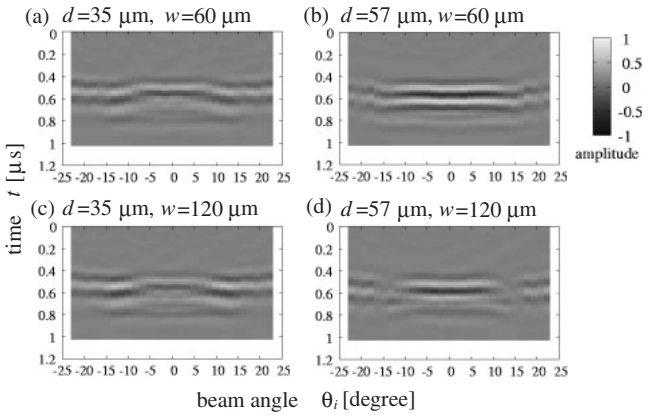

Fig. 16. Angular dependences from gaps calculated on the basis of superposition principle.

whose depth d is about 30 μm were simulated by superposition of those from a step whose height d is 35 μm. Similarly, the angular dependences of echoes from a gap whose depth d is about 60 μm were simulated by superposition of those from a step whose height d is 57 μm.

Figure 16 shows the simulated angular dependences of echoes from gaps calculated on the basis of the superposition principle. The simulated angular dependences of echoes shown in Figs. 16(a)–16(d) correspond to those measured for objects Nos. 4–7 shown in Figs. 11(b)–11(e), respectively. As shown in Fig. 16, the echo amplitudes in the region where the beam angle θ_i is about 0° of the object with a height d of 57 μm are larger than those of the object with a height d of 35 μm. Furthermore, echo amplitudes in the range $|\theta_i| \geq 15°$ increase as the width w of a gap increases. These results well correspond to those shown in Fig. 11. Therefore, the angular dependences of echoes from a gap on a surface can be considered from those of echoes from a step.

5. Applying Angular Dependences to Estimation of Surface Roughness

5.1 Objects

Four metal plates that have different surface roughnesses obtained by polishing with sandpaper were measured. Figure 17 shows the surface profiles $h(x_i)$ at lateral position x_i of objects Nos. A–D measured by the stylus method. Figure 18 shows the conventional linear scanning B-mode images of objects Nos. A and D. As shown in Fig. 18, the surface profile $h(x_i)$ in the micron-order shown in Fig. 17 cannot be detected by the conventional B-mode imaging using linear scanning.

In this study, the rms roughness Rq, which is the standard deviation of the surface height $h(x_i)$, is used for the statistical evaluation of surface roughness. The rms roughness Rq is obtained as follows:

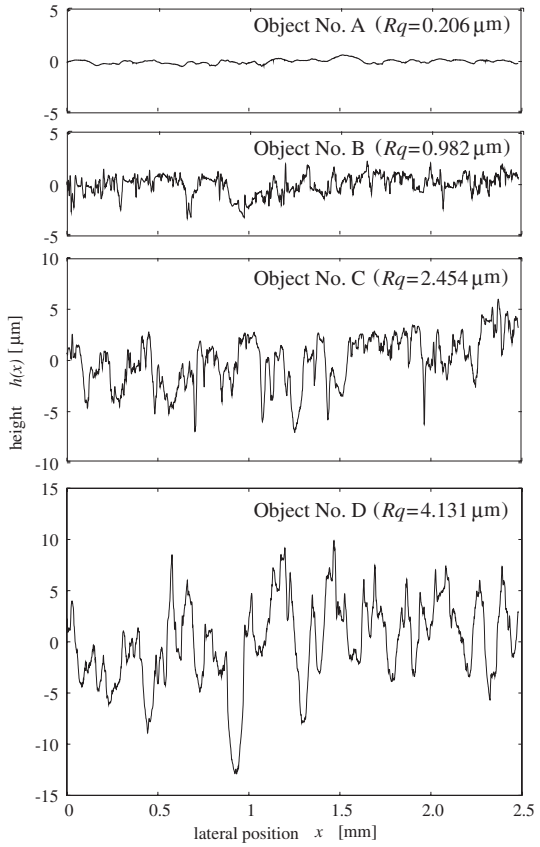

Fig. 17. Surface profiles of objects Nos. A–D measured by the stylus method.

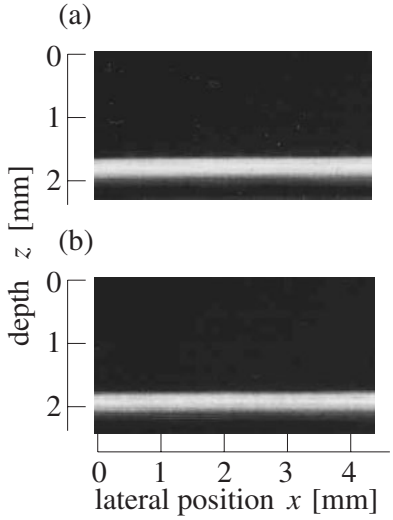

Fig. 18. Conventional B-mode images of objects No. A (a) and No. D (b).

$$Rq = \sqrt{\frac{1}{N}\sum_{i=0}^{N-1}\left\{h(x_i) - \overline{h(x)}\right\}^2}, \tag{5.1}$$

where N is the total number of lateral positions $\{x_i\}$ and $\overline{h(x)}$ is the average height of the surface profile. Figure 17 also shows Rq of each object used in these measurements.

5.2 Estimation of surface roughness

Figures 19(a) and 19(b) show RF echoes from object No. A ($Rq = 0.206$ μm), which has the most smooth surface

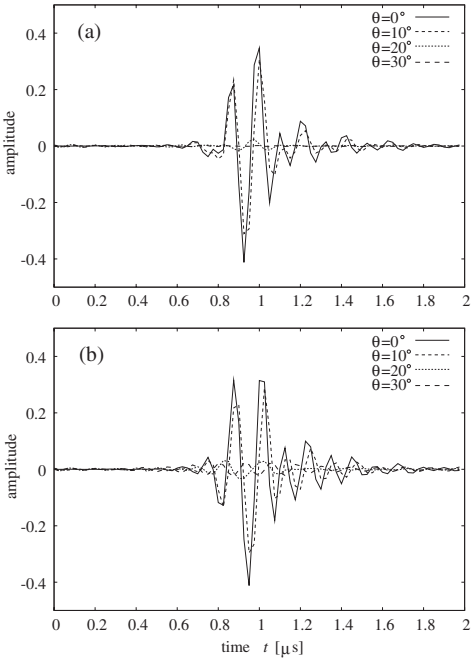

Fig. 19. RF echoes from objects No. A (a) and No. D (b).

among the measured objects in these experiments, and from object No. D ($Rq = 4.131\,\mu\text{m}$), which has the roughest surface, respectively. In these experiments, the distance l from the surface of the probe to the surface of the object was set to be 9.4 mm, and the maximum beam angle $\theta_{\max}$ was 32.6°. As shown in Fig. 19(a), in the case of the smooth surface, the amplitude of RF echo at the beam angle $\theta = 20^\circ$ is low and that at the beam angle $\theta = 30^\circ$ cannot be detected. On the other hand, in the case of the rough surface, the amplitude of RF echo at the beam angle $\theta = 30^\circ$ can be detected as shown in Fig. 19(b). These results correspond to the case in which the amplitudes of echoes from surfaces with gaps are larger in the range $\theta \geq 20^\circ$ than those from the smooth surface as shown in Fig. 11. From these results in Fig. 19, the echo amplitudes in the range $\theta \geq 20^\circ$ increase as the surface of the objects becomes rough.

The angular dependences of ultrasonic echoes from four different objects that have different surface roughnesses, as shown in Fig. 17, were measured and the power spectra of RF echoes at the corresponding beam angles $\{\theta_i\}$ were acquired. In these experiments, the experimental system is similar to the system shown in Fig. 1. The angular dependences of RF echo were measured by moving the ultrasonic probe automatically using a stage. RF echoes were acquired during 4 mm movement at 10 μm intervals (the number of measurement points $\{x_i\} = 400$).

Figure 20 shows the averaged power spectra of RF echo at each beam angle θ for each object shown in Fig. 17. As shown in Fig. 20, for the beam angle θ of about 0°, the power spectra shown in Figs. 20(a)–20(d) are similar whereas the surface roughness Rq differs. However, in the case of $\theta \geq 20^\circ$, the center frequency component increases as surface roughness Rq increases.

Figure 21 shows the power spectra shown in Fig. 20 for the temporal frequencies from 5 to 10 MHz. As shown in Figs. 21(c)–21(e), the power spectra at about the center frequency ($f = 7.5$ MHz) increase as surface roughness Rq

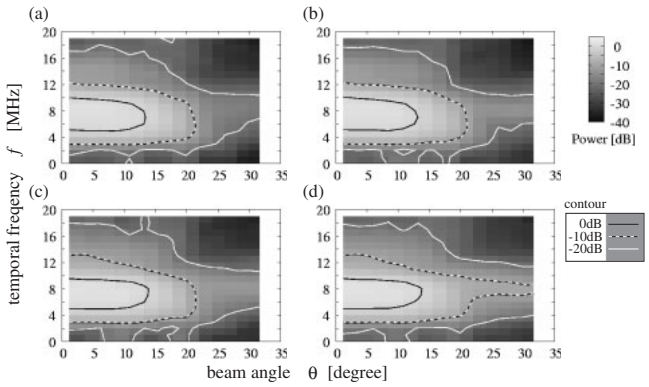

Fig. 20. Average power spectrum of RF echo at each beam angle θ_i for each object shown in Fig. 17.

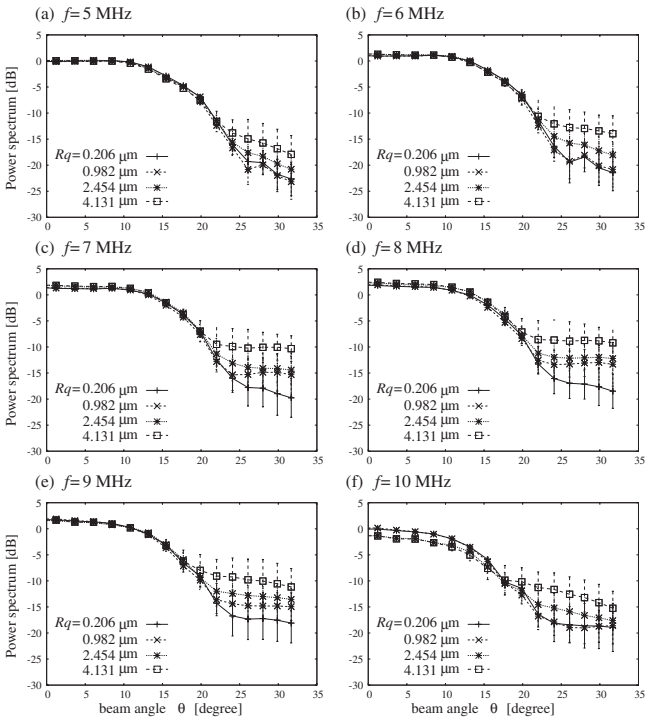

Fig. 21. Power spectra at $f = 5$ MHz (a), $f = 6$ MHz (b), $f = 7$ MHz (c), $f = 8$ MHz (d), $f = 9$ MHz (e), and $f = 10$ MHz (f).

increases when the beam angle θ is greater than 20°. The power of RF echo, $P(\theta)$, is obtained as follows:

$$P(\theta) = \frac{1}{N}\sum_{i=0}^{N-1}\sqrt{\left\{V_\theta(t) - \overline{V_\theta(t)}\right\}^2}, \tag{5.2}$$

where $V_\theta(t)$ is the RF echo signal at time t and $\overline{V_\theta(t)}$ is its average. Figure 22 shows the changes in the power $P(\theta)$ of RF echo at the corresponding beam angles θ for all objects. In Fig. 22, the power $P(\theta)$ of RF echo is normalized by the power $P(0^\circ)$ at $\theta = 0^\circ$. As shown in Fig. 22, the normalized power $P(\theta)/P(0^\circ)$ of RF echo in the region of $\theta \geq 20^\circ$ increases as the surface roughness Rq increases. The relationship between the surface roughness Rq and the normalized power $P(\theta)/P(0^\circ)$ of RF echo is shown in Fig. 23. From Fig. 23, it is found that the increase in the surface roughness Rq causes the increase in the power of RF echo in the region of $\theta \geq 20^\circ$.

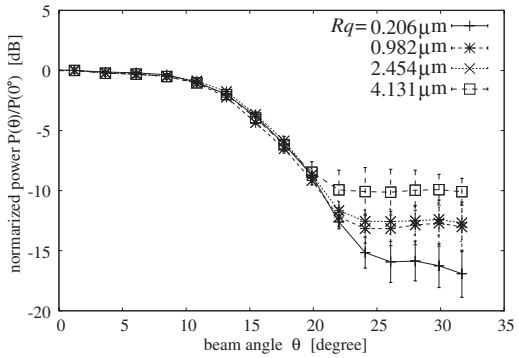

Fig. 22. Changes in the normalized power $P(\theta)/P(0^\circ)$ of RF echoes at corresponding beam angles θ for all objects.

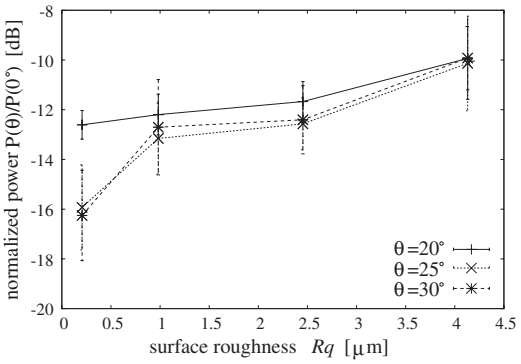

Fig. 23. Relationship between the surface roughness Rq and the normalized power $P(\theta)/P(0^\circ)$ of RF echo in the range $\theta \geq 20^\circ$.

6. Conclusions

In this study, the angular dependence of ultrasonic echoes was measured by steering the ultrasonic beam. Objects that have a micron-order step and gap that cannot be detected by conventional B-mode imaging using linear scanning were used in these measurements. Using the proposed method, it was found that the spatial distribution of echo amplitude and the frequency characteristics of echo in both temporal and spatial domains differ as the surface profile differs. Furthermore, using the proposed method, it was shown that the increase in the surface roughness Rq causes the increase in the power of RF echo in the region of $\theta \geq 20^\circ$. These results provide a possibility that a micron-order surface roughness can be quantitatively evaluated using the angular dependence of ultrasonic echo.

1) P. C. G. Simons, A. Algra, M. L. Bots, D. E. Grobbee, and Y. van der Graaf: Circulation **100** (1999) 951.
2) T. Mashiyama, H. Hasegawa, and H. Kanai: Jpn. J. Appl. Phys. **45** (2006) 4722.
3) R. T. Lee, A. J. Grodzinsky, E. H. Frank, R. D. Kamm, and F. J. Schoen: Circulation **83** (1991) 1524.
4) H. Kanai, M. Sato, Y. Koiwa, and N. Chubachi: IEEE Trans. Ultrason. Ferroelectr. Freq. Control **43** (1996) 791.
5) H. Hasegawa, H. Kanai, N. Hoshimiya, and Y. Koiwa: J. Med. Ultrason. **31** (2004) 81.
6) H. Kanai, H. Hasegawa, M. Ichiki, F. Tezuka, and Y. Koiwa: Circulation **107** (2003) 3018.
7) J. Inagaki, H. Hasegawa, H. Kanai, M. Ichiki, and F. Tezuka: Jpn. J. Appl. Phys. **44** (2005) 4593.
8) J. Inagaki, H. Hasegawa, H. Kanai, M. Ichiki, and F. Tezuka: Jpn. J. Appl. Phys. **45** (2006) 4732.
9) R. Ross: New Engl. J. Med. **340** (1999) 115.
10) M. C. Corretti, T. J. Anderson, E. J. Benjamin, D. Celermajer, F. Charbonneau, M. A. Creager, J. Deanfield, H. Drexler, M. Gerhard-Herman, D. Herrington, P. Vallance, J. Vita, and R. Vogel: J. Am. College Cardiol. **39** (2002) 257.
11) M. Sugimoto, H. Hasegawa, and H. Kanai: Jpn. J. Appl. Phys. **44** (2005) 6297.
12) T. Reichlin, A. Wild, M. Dürrenberger, A. U. Daniels, U. Aebi, P. R. Hunziker, and M. Stolz: J. Struct. Biol. **152** (2005) 52.
13) D. D. Sukmana and I. Ihara: Jpn. J. Appl. Phys. **44** (2005) 4417.
14) D. D. Sukmana and I. Ihara: Jpn. J. Appl. Phys. **45** (2006) 4534.
15) C. Arihara, H. Hasegawa, and H. Kanai: Jpn. J. Appl. Phys. **45** (2006) 4727.
16) N. Nakagawa, H. Hasegawa, and H. Kanai: Jpn. J. Appl. Phys. **43** (2004) 3220.